Thin Layer Lightweight and Ultrawhite Hexagonal Boron Nitride Nanoporous Paints for Daytime Radiative Cooling

Andrea Felicelli†, Ioanna Katsamba†, Fernando Barrios, Yun Zhang,
Ziqi Guo, Joseph Peoples, George Chiu**, Xiulin Ruan*

School of Mechanical Engineering and Birck Nanotechnology Center,
Purdue University, West Lafayette, IN, USA

† These authors contributed equally to this work
Corresponding Author E-mail: ruan@purdue.edu*, gchiu@purdue.edu**
Lead Contact: ruan@purdue.edu*

Summary

Thin and lightweight radiative cooling paints are needed for many weight-sensitive applications. However, it is difficult to achieve high solar reflectance with thin layers. This work develops ultrawhite hBN-Acrylic paints that achieve solar reflectance of 97.9% and sky window emissivity of 0.83 with only 150 μm thickness and 0.029 g/cm^2 weight, representing significant reductions from previous radiative cooling paints. The high refractive index and nanoplatelet morphology of hBN enable a unique combination of Mie scattering-like high scattering coefficient and Rayleigh scattering-like strong backscattering, and a porosity of 44.3% offers high refractive index contrast between hBN and air - all contribute to achieve high solar reflectance with a thin coating. Field tests show full daytime cooling under direct sunlight, reaching 5-6°C below ambient on average during daylight hours. Our hBN-Acrylic paint demonstrates comparable cooling performance to

recent best technologies, and the thinness and lightweight reduce barriers towards many practical applications.

Introduction

According to the United States Department of Energy, 6% of the average household's energy use goes towards space cooling (US Department of Energy, 2014). This is due to cooling technologies that rely on electricity generated via processes with high carbon emissions. At a time when many are interested in working to address climate crisis affecting our planet, it is vital to look into ways to reduce our carbon-footprint in everyday life. Radiative Cooling is a passive cooling technology that accomplishes this by reflecting solar irradiation and emitting thermal radiation via an atmospheric transparent window (a wavelength range of 8-13 microns) into deep space, therefore not relying on electricity generation (Barker, 1875). When a material emits more heat in the sky window than it absorbs from the solar irradiation, the resulting net cooling power allows for cooling the surface on earth to a temperature below the surrounding ambient. Conventional air conditioning removes heat from buildings into the ambient air (Munday, 2019) so heat still stays in the city and on the earth. Radiative cooling, on the other hand, directly loses heat to the deep space, reducing the heat island effect and cooling down the earth.

Radiative cooling coating and composite technologies have greatly advanced throughout the years. In one of the earliest studies on paints for radiative cooling, a thin commercial titanium oxide-based paint layer was coated on an aluminum plate to achieve daytime radiative cooling (Harrison and Walton, 1978). However, the high solar reflectance was mostly from the metal substrate and not the paint itself, i.e., no substrate-independence was demonstrated. Another study measured the radiative cooling performance of several commercially available white paints (Orel,

Gunde and Krainer, 1993). There have also been heat reflecting paints developed reaching 91% reflectance (Pockett, 2010). These early studies on paints showed the need for improved solar reflectance in paints in order to reach full daytime cooling.

Some other approaches to radiative cooling have involved non-paintable technologies. Outside of explicit radiative cooling considerations, sintered reflective ceramic coatings consisting of Al_2O_3, hBN, and other particles were pursued for space applications and achieved spectral reflectance of 87.5% (Holynska et al., 2019). In the last decade, full daytime radiative cooling has been achieved in photonic materials, such as integrated photonics solar reflectors and thermal emitters with several layers of silicon oxide and hafnium oxide (Raman et al., 2014), polymer coated, fused silica mirrors (Kou et al., 2017), resonant polar dielectric microspheres embedded in a polymer matrix with a metallic bilayer (Zhai et al., 2017), structural materials consisting of delignified and densified wood (Li et al., 2019), pressed nanocomposite films embedded with hBN (Yang et al., 2021), (Li et al., 2021), with the latter achieving 98% solar reflectance at a rather thick film of 1.4mm (Li et al., 2021), and other photonic and multilayer structures (Rephaeli, Raman and Fan, 2013). However, these approaches have one or more limitations such as complicated multi-layered structures, a metallic layer, or large thickness of more than 1 mm to achieve the needed solar reflectance. Meanwhile, although radiative cooling films often have end components of particles and polymers, which are similar to that of paints, they are not paintable technologies hence limiting their applications. In this scenario, radiative cooling film technologies and paint technologies should not be mixed, because a film technology usually cannot transit to a paint technology, or at least involve significant barriers to be resolved. Cooling paints, defined as being applicable using standard brush, roller, or spray-painting techniques, are desired to allow for ease of use and viable applications on non-flat surfaces, compared to films.

For this reason, there is a renaissance of radiative cooling paint technology recently. A double-layer acrylic coating embedded with titanium dioxide and carbon black nanoparticles was predicted to achieve full-daytime cooling (Huang and Ruan, 2017). Silica microsphere media without a binder were tested to show partial daytime cooling (Atiganyanun et al., 2018), and paint-like porous polymeric coatings with 5.5 μm and 200 nm pore sizes were developed with full-daytime cooling (Mandal et al., 2018). Further, a strategy of broad particle size distribution was proposed to enhance the solar reflectance than a single size (Peoples et al., 2019). Recently, high concentration $CaCO_3$ and $BaSO_4$-based paints have been developed with high solar reflectance and sky window emittance, that can achieve full daytime radiative cooling capabilities (Ruan et al., 2020), (Li et al., 2020), (Li et al., 2021). $BaSO_4$ has high band gaps of 7.27 eV that can eliminate the UV absorption, and the high concentration and broad particle size distribution enable broadband high solar reflectance. It was also suggested that the average particle size should be in the neighborhood of the peak solar wavelength (500 nm), and these sizes are more effective in scattering the sunlight than particle or pore size that is either too small (<100 nm) or too large (>1 μm) (Huang and Ruan, 2017), (Peoples et al., 2019), (Ruan et al., 2020), (Li et al., 2020), (Li et al., 2021). While high performance and greater ease of use have been demonstrated with paint technologies like these, they required 300 μm thickness to reach 96% solar reflectance in the porous polymer coatings (Mandal et al., 2018), and 400 μm thickness to reach the highest reported solar reflectance of 98.1% in $BaSO_4$ paint, the whitest paint reported to date (Li et al., 2021). Other ultra-white paints may need mm thickness to reach optimal performance (Mandal et al., 2020). In contrast, typical commercial paint thickness is 120 microns on vehicles and 150-200 microns on buildings, and each coat by brush or roller adds 50-75 microns of paint when dried. The much larger thickness of current radiative cooling paints would mean 5-8 coats and much more labor.

Moreover, the density of $BaSO_4$ (4.5 g/cm^3) is higher than the commercial TiO_2 (4.23 g/cm^3). Therefore, the best radiative cooing paints represent significantly higher thickness and weight than commercial paints currently in use, and perhaps too high for many important applications that are weight-sensitive, such as automobiles, wearables, aerospace, and space applications. Considering these barriers, there remains an urgent need to develop high-performance but significantly thinner and/or lighter radiative cooling paints. This is a very challenging task as it means the backscattering coefficient needs to be remarkably enhanced as compared to the state of the art.

In this work, we have designed and fabricated thin and light-weight hBN-Acrylic nanoporous paints, on which we have experimentally demonstrated the high solar reflectance and sky window emissivity, and full daytime subambient cooling. A provisional patent based on this work was filed with the United States Patent & Trademark Office (USPTO) on August 28, 2021 with the application number 63238124. The hBN in a nanoplatelet form was chosen due to its appropriate band gap and unique morphology. The upper bound of the photon energy in the solar spectrum is 4.13eV, hence the material band gap needs to be higher than 4.13 eV to eliminate solar absorption. However, as the band gap increases, the refractive index decreases which weakens scattering and reflection. Therefore, a band gap moderately higher than 4.13 eV is preferred (Tong et al., 2022). hBN has band gap of 5.96 eV which is above 4.13 eV but significantly lower than that of $BaSO_4$, resulting in a refractive index of 2.1-2.3 in the solar spectrum when BN planes are oriented parallel to the electric field (hereafter called “in-plane” orientation, or perpendicular to the incident wave) and 1.4-1.6 when BN planes are vertical to the electric field (or parallel to the incident wave) (McKay et al., 2020), (Lee et al., 2018). In contrast, the refractive index is only 1.66 for $BaSO_4$ (Tong et al., 2022). Our simulations also show that the higher refractive index and nanoplatelet morphology for hBN yield an unusual combination of Mie scattering-like high

scattering coefficient and Rayleigh scattering-like strong backscattering, both of which favor high solar reflectance. Furthermore, the nanoplatelets used had a diameter of 332 ± 193 nm, where the average diameter is optimum to strongly scatter the solar spectrum and the non-uniform diameter distribution enables efficient broadband scattering as compared to a single size (Peoples et al., 2019), (Golla et al., 2013). A high nanoplatelet loading of 60% volume concentration (Hereafter it means the volume concentration among the solid phases in the wet paint phase if not otherwise stated. After the paint is dried, the layer develops a porosity of 0.443, hence the volume concentrations of hBN, acrylic, and air become 33.4%, 22.3%, and 44.3% respectively) is used to maximize light scattering while maintaining the desirable mechanical properties of the polymer binder. With this concentration, we achieved 97.9% reflectance in the solar spectrum and a sky window emissivity of 0.83 from a dried paint layer with a thickness of only 150-micron and weight of only 0.029 g/cm^2. Outdoor testing showed an average of 5-6 degrees Celsius cooling below ambient on the sample's surface. The thickness and weight are significantly lower than previous records of radiative cooling paints, while maintaining a solar reflectance among the highest. The thickness is now reduced to the typical range of commercial paints, and the light weight is attractive for weight-sensitive applications, such as automobiles, wearables, aerospace and space applications. Furthermore, it has wear-resistance, viscosity, and water resistance consistent with that of industry standards at only a fraction of the layer thickness.

Results and Discussions

Paint Fabrication and Characterizations

First, we have designed and fabricated hBN-Acrylic coatings with a range of different thicknesses. Since a high concentration is desirable to promote effective light scattering within the

material, the paint was loaded with hBN nanoplatelets at hBN : Acrylic = 60% : 40% volume concentration. Samples were prepared by pouring or brushing uniform layers onto flat glass or aluminum substrates and allowed to fully dry in a fume hood. The resulting samples are visibly ultrawhite and opaque, with consistent layer thickness distributions across substrates. Figure 1a illustrates the techniques used in this research, as well as an example of the paint layer tested throughout.

SEM imaging was used to determine nanoplatelet morphology, orientation, and observe their dispersion throughout the acrylic matrix. The nanoplatelet structure of the hBN has a high aspect ratio and directional properties, as well as a high degree of variability in diameter and low variability in thickness (Figure 1b). An overall diameter distribution of 332 $\pm$ 193 nm (Figure 1c) and a fairly uniform distribution of platelet thickness of 45 $\pm$ 3 nm (Figure 1b) are observed, which should contribute to improved light scattering and higher solar reflectance values as a result. This is due to an average size in the neighborhood of the solar peak wavelength and a broad size distribution (Golla et al., 2013). The acrylic matrix that encapsulates and bonds the nanoplatelet filler gives the material improved reliability under various conditions due to the polymer-filler composition similar to the majority of commercially-available paints, although with a higher pigment loading (Figure 1d). The platelets can be observed to be in various orientations. Some horizontal orientation may be achieved due to the shear force effects of pouring techniques, where the paint is allowed to flow vertically downwards along the substrate due to gravitational effects, or brushing/screen-printing techniques, where the equipment distributes the paint directionally along the substrate surface. This orientation, with the surface of the platelet perpendicular to incident sunlight, allows the larger refractive index of the hBN to take effect and enable efficient scattering (McKay et al., 2020). Although there remain some particles that can be observed to be

at a more angled orientation (Figure 1d), high radiative cooling performance is still achieved. This suggests desired performance can be achieved without perfect particle alignment. DMF is added to the mixture at a 1:6 volume ratio, which was found to reduce viscosity associated with the high concentration of nanoplatelets to a usable level while maintaining low evaporation time of 2-4 hours depending on coating thickness. The average porosity of a dried paint layer is calculated to be 44.3% with a standard deviation of 1.4%. The pores can facilitate strong scattering and reduce the paint layer thickness needed, since they enable hBN-air interfaces with high refractive index contrast (n_{hBN} : n_{air} = 2.3:1). In contrast, porous polymers (Mandal et al., 2018) or fully dense hBN-PDMS photonic films without voids (Li et al., 2021) do not have such high contrast. It should be noted that the volume concentrations of hBN and acrylic are 60% and 40% among the solid phases in the wet paint state; after the paint is dried with a porosity of 44.3%, the volume concentrations of hBN, acrylic, and air become 33.4%, 22.3%, and 44.3% respectively. Although it's acknowledged that the porosity can lead to soiling of the material over time in application, it is recommended that a hydrophobic, self-cleaning topcoat is used. The use of topcoats is a well-established technique and is already very frequently used to address this issue for commercial paints in outdoor applications. Alternatively, binders that show strong hydrophobic properties can also be promising. Details on the porosity calculation can be found in the Experimental Procedures section.

Optical Property Characterization and Modeling

Radiative cooling performance including daytime subambient cooling is optimized in materials by achieving high reflectance in the solar spectrum of 250-2500 nm and a high emittance in the sky window of 8-13 μm. In coatings and paints, this can be done by designing the material

based on the properties of the nanoparticle filler and matrix. The acrylic matrix not only helps to provide ease of use and improved reliability in application, but also contributes to the high sky window emissivity. The hBN-Acrylic coatings showed excellent solar reflectance at various layer thicknesses. At 150 microns, the coating's solar reflectance begins to saturate at 97.9% and the emissivity is measured to be 0.83 (Figure 2a). At 70 microns, the solar reflectance is still 90.9% and the sky window emissivity is 0.78 (Figure 2b). Figure 2c shows the solar reflectance measured as a function of thicknesses, including 91.6%, 92.1%, 93.0%, 95.0%, and 98.2% for 80, 110, 120, 130, and 350 micron-thick coatings, respectively. Saturation of reflectance at higher coating thickness, as seen in Figure 2c, demonstrates that for maximum solar reflectance, the coating does not need to be thicker than 150 microns. Figure 2c also shows that at 150 µm thickness, our hBN-Acrylic nanoporous paint achieves comparable or higher solar reflectance than previous best radiative cooling paints, films, and porous polymers (Li et al., 2021), (Mandal et al., 2018), (Ruan et al., 2020), (Li et al., 2020), (Li et al., 2021), but the thickness is reduced by 50% or more. Further, the density of hBN is only 2.1g/cm^3, which is less than half of $BaSO_4$ at 4.5g/cm^3. Hence the weight of the hBN-Acrylic coating is much reduced from previous cooling paints (a detailed compassion is given later in the paper). Moreover, at 350 microns, 50 microns less than the 400 micron thickness required to reach 98.1% in previous work (Li et al., 2021), we measured 98.2% solar reflectance. Our measured solar reflectance values are also significantly higher than commercial heat-reflective paints (Pockett, 2010). Figure 2d shows a comparison between the experimental solar reflectance with Monte Carlo simulation data, which will be described in detail subsequently.

To explain the ultra-high solar reflectance achieved for such a thin paint layer, the scattering coefficient and asymmetry parameter are calculated for hBN nanoplatelets using

COMSOL, and the results are compared to those for $BaSO_4$ spherical nanoparticle in Figs. 3a and 3b. The refractive indices are given in Figure S1 and the validation of the COMSOL model against the Mie theory is shown in Figure S2 in the supplementary material. Both nanoparticles have the same diameter of 370 nm, while the thickness of the platelets is 50 nm. Figure S3 shows the simulation setup for the scattering coefficient in COMSOL and the solar reflectance with Monte Carlo simulations. It is very interesting to note that hBN nanoplatelets show higher scattering coefficient (Figure 3a) and lower asymmetry parameter (i.e., more backscattering) (Figure 3b and 3c) in the in-plane direction in the entire spectrum than spherical $BaSO_4$, the previous state-of-the-art. This result is significant and surprising. The asymmetry parameter gives important insights related with the form of scattering. It is close to unity when the backscattering is very narrow; this is known as geometric scattering. In contrast, the asymmetry parameter is close to zero when Rayleigh scattering occurs. For spherical particles, Mie scattering is usually favorable for achieving high reflectance because it provides a high scattering coefficient. However, a drawback is in the weaker backscattering. On the other hand, Rayleigh scattering offers equal backward and forward scattering; however the scattering coefficient is too small. A natural question is whether the high, Mie scattering-like scattering coefficient and the strong, Rayleigh scattering-like backscattering can be achieved simultaneously. Clearly it is not feasible with spherical particles. However, this is achieved with the proposed hBN nanoplatelets. Further comparison between the asymmetry parameter of platelet-shaped particles and the spherical particles is given in Figure S4. The backscattering coefficient of two imaginary particles, spherical hBN and platelet $BaSO_4$, is also studied to systematically understand the respective roles of the refractive index and the particle morphology. The spherical hBN has a higher scattering coefficient than the platelet hBN; however, the platelet-shaped particle's lower asymmetry parameter results in a stronger backscattering

coefficient in the ultraviolet, visible, and infrared wavelengths (Figure 3c), indicating that the platelet morphology is favorable than the spherical one, aside from refractive index. The results indicate that higher refractive index enhances the scattering coefficient, and the nanoplatelet morphology compromises the scattering coefficient slightly but overall enhances backscattering and eventually the backscattering coefficient, as compared to $BaSO_4$ spherical nanoparticles.

As for the platelet orientations, the scattering coefficient (Figure 3d), asymmetry parameter (Figure 3e), and back-scattering coefficient (Figure 3f) are studied for both the in-plane and cross-plane orientations, as well as a 45-degree angle between them. As expected, the angled orientation is overall lower in all values compared to the in-plane (horizontal) orientation and higher than the cross-plane (vertical) orientation.

Figure 3g shows the backscattering coefficient of hBN of various sizes (diameter of 100, 200, 400 and 800 nm with constant thickness of 50nm). Once more, it is observed that each nanoplatelet diameter peaks the backscattering coefficient at distinct wavelength bands, implying the high variability in nanoparticle sizes can enhance the total reflectance (Peoples et al., 2019). Surprisingly, Rayleigh scattering-like asymmetry parameter is detected for hBN nanoplatelet at most of the regions including visible and infrared spectrum, regardless of size resulting in prominent backscattering. This is favorable for high solar reflectance.

The total reflectance of the four particles in Figs. 3(a)-(c) is also calculated by using the Monte Carlo method, and the results are shown in Figure 3h. The solar reflectance in the order from high to low are nanoplatelet hBN, spherical hBN, nanoplatelet $BaSO_4$, and spherical $BaSO_4$, indicating both high refractive index and nanoplatelet morphology favor high solar reflectance and explain why hBN nanoplatelet-acrylic paints outperform $BaSO_4$-acrylic paints in solar reflectance. The simulated solar reflectance on the nanoplatelet hBN agree with the experimental data

reasonably well, as shown in Figure 2d. It is essential to mention the assumptions used to simplify the Monte Carlo model. No air pores were included in the nanocomposite as was observed from the SEM images, and nanocomposite consists of only single-size particles. These could result in an underprediction of total reflectance. On the other hand, our Monte Carlo method only uses scattering coefficient of light vertically incident on the hBN nanoplatelets while no angular dependency is considered. This would cause overprediction of scattering and reflectance for an anisotropic material like hBN platelets. The agreement of the total solar reflectance between our experiment and Monte Carlo simulations, despite of capturing the main physics, can be partly due to error cancellation and hence should be interpreted with caution.

Cooling Performance Tests and Analysis

The sky window emissivity for hBN-Acrylic paints, at a value of 0.83, is relatively lower due to the lack of the sky window infrared-active phonon modes that contributes to emissivity in $BaSO_4$-Acrylic paints. However, during the daytime the sky window emissivity has much smaller role than the solar reflectance, and this is explained as follows. The overall radiative cooling capabilities of materials can be more fairly compared using the previously developed RC Figure of Merit (Li et al., 2020), defined as:

$$RC = \varepsilon_{sky} - r(1 - R_{solar})$$

In this equation, ε_{sky} is the total sky window emissivity, r is the ratio of solar irradiation power over the blackbody surface emissive power in the sky window and is recommended to be set as ~7.14, assuming a standard 1000 W/m^2 solar irradiation power and 140 W/m^2 blackbody surface emissive power in the sky window, and R_{solar} is the total solar reflectance. The physical meaning of RC is simple, that its multiplication with the blackbody surface emissive power in the

sky window would yield the net radiative cooling power. From this definition, every 0.01 increment in the solar reflectance is equivalent to 0.0714 increment in the sky window emissivity in terms of the cooling performance. This figure of merit shows that cooling below ambient can in principle be achieved when RC is positive. For an hBN-Acrylic layer of 150 micron thickness, the RC is calculated at 0.68, demonstrating 68% radiative cooling capability over the theoretical limit. This is calculated from the 97.9% total solar reflectance measured for a 150-micron layer on a 1-mm glass substrate, and the 0.83 sky window emissivity calculated from measurements for a 150-micron layer on a 1-mm aluminum substrate. This can be compared to previous RC figures of merit for TiO_2-Acrylic, $CaCO_3$-Acrylic, $BaSO_4$ films, and $BaSO_4$-Acrylic paint of 0.18, 0.62, 0.79, and 0.82 respectively (Li et al., 2021). It can also be compared to recent non-paintable approaches, which show RC's of 0.32 (Raman et al., 2014), 0.53 (Zhai et al., 2017), 0.35 (Kou et al., 2017), and 0.57 (Mandal et al., 2018). The RC for hBN-Acrylic paints is among the highest calculated.

Furthermore, as a method to compare the performances of different materials while normalizing to layer thickness, a modified form of the originally given Figure of Merit is proposed:

$$RC_t = [\varepsilon_{sky} - r(1 - R_{solar})](1 - t/t_o),$$

where RC_t is the radiative cooling figure of merit with thickness taken into consideration, t is the layer thickness, and t_o is the maximum considered layer thickness (1 mm is recommended, as radiative cooling coatings are typically engineered to be below this thickness). This figure of merit is a rough approximation, and a truly accurate figure would likely involve a much more complicated expression. However, it can be used to roughly compare different materials. Using 1.5 mm for t_o, RC_t is calculated for various materials: 0.453 for $CaCO_3$-Acrylic Paints, 0.132 for TiO_2-Acrylic Paints, 0.701 for $BaSO_4$ films, 0.597 for $BaSO_4$-Acrylic Paints, and 0.612 for the studied hBN-Acrylic Paints.

Outdoor testing was performed to demonstrates the radiative cooling capability of the hBN-Acrylic coatings. The test setup is shown in Figure 4a and the details are given in the Methods section. The ambient temperatures during outdoor tests vary between 20-30 °C and the sample temperature is consistently lower than the ambient during daytime and nighttime (Figure 4b). Over the 3 days, an average temperature difference from the ambient was achieved of 6-8 °C overall and 5-6 °C during daylight hours (Figure 4c). Under the peak solar irradiation of 1,063 W/m^2, the sample can remain ~1-2 °C cooler than the ambient owing to the high solar reflectance. The total sky window emittance of 0.83 results in a maximum temperature difference of 12 °C observed during the clear night on July 26th, 2021. This experiment was further validated through comparison to a thermal balance model, described in detail in Note S1, Table S1, and Figure S5.

Reliability Tests and Viscosity Characterization

A vital aspect of radiative cooling coatings is the feasibility of application, as well as the durability in outdoor use. Our 60% hBN-Acrylic samples, made to 150 micron layer thickness on 1-mm aluminum sheet substrates, were subjected to several tests to demonstrate adequate performance in these regards. In Figure 5a, the samples are tested for mass-loss while undergoing 2000 cycles of abrasion testing. Over this range, the mass loss experienced by the hBN-Acrylic coating is comparable with that of commercial white paint, and slightly outperforms previously developed calcite paints (Li et al., 2020). These results show that the wear of the developed coatings is similar to materials currently in use, and therefore demonstrate that the proposed material meets existing material performance in its resistance to mass loss from abrasion. Another aspect of concern in outdoor use is exposure to water. The hBN-Acrylic coating samples were tested for water resistance by being submerged in circulating water for 24 hours. The samples were

weighed before the experiment, as well as after 24 hours of drying time in the fume hood after the experiment. A net-zero mass loss was calculated, demonstrating good water resistance (ASTM Subcommittee D01.27, 2020).

To demonstrate ease and versatility of application techniques for the hBN-Acrylic coatings, a viscosity test was carried out and result were compared to commercial paints (Whittingstall, 2011) and the previously developed barite paint (Li et al., 2021). The viscosity was measured at constant sample temperature throughout and at various shear rates in the range of 50 and 500 s^{-1}. As illustrated in Figure 5b, the hBN-Acrylic paint showed slight shear thinning, as well as a relatively lower viscosity compared to other paints. However, it remains within the industry recommended range of viscosities for brushing application of paints and coatings (Whittingstall, 2011).

Thinness, Light Weight, and Their Significant Benefits

For easier comparison, Table 1 shows properties of various materials proposed in literature as well as those of the hBN-Acrylic paints proposed in this work. Compared to the $BaSO_4$-Acrylic paint that shows 98.1% solar reflectance (Li et al., 2021), the hBN-Acrylic paint here shows 97.9% solar reflectance but the thickness and weight are reduced by 62.5% and 78.4% respectively. Even when compared to the porous polymers that show 96% solar reflectance (Mandal et al., 2018), our hBN-Acrylic paint shows higher solar reflectance while the thickness and weight are still reduced by 50% and 45.3% respectively. It should be noted that the $BaSO_4$-Acrylic paint (Ruan et al., 2020), (Li et al., 2021) and CaCO3-Acrylic paint (Ruan et al., 2020), (Li et al., 2020) were porous too, but their porosity is unknown at this time hence not counted in calculating their density, which would otherwise decrease to some extent. However, it remains clear that the hBN paint has the

advantage in lowest thickness, lowest weight, and among the highest solar reflectance and quite high sky window emissivity, resulting in having the highest RC_t value amongst the compared materials.

It is noted that the cost of hBN nanoplatelets is higher than that of $BaSO_4$ nanoparticles. However, there is still significant benefit to a lightweight, thin paint layer of hBN in weight-sensitive applications requiring radiative cooling, such as aerospace technologies, airplanes, vehicles, and wearable technology. In wearables, typically only a small amount of lightweight coating is needed. In aircraft, seemingly small reductions in weight can result in significant decreases in fuel consumption and related CO_2 emissions. For example, we estimate that if the hBN-Acrylic paint rather than $BaSO_4$-Acrylic paint is used on all the 23,000 airplanes in operation globally, the total fuel savings would be 340,000 metric tons and the CO_2 emission reduction would be ~ 1 million metric tons on a yearly basis. More details on this estimate can be found in Note S2.

In terms of the thickness, each coat by brush or roller only adds 50-75 microns of paint when dried and more than 5-8 coats would be needed to reach 400 μm or mm-thick layers that have previously been needed. With the 150 micron hBN paint introduced in this work, the thickness of radiative cooling paints is brought to the common practical range, and only two coats are needed on average.

For the above reasons, the light weight and thinness are a significant innovation within this work. It provides a feasible option for a critical challenge of radiative cooling paints in many practical applications. The thin, lightweight ultra-white paint introduced in this work is expected to make a major impact in the field.

In this work, we have designed and fabricated a low density, high concentration nanoplatelet-based hBN-Acrylic nanoporous paint and experimentally demonstrated their radiative cooling performance at low coating thickness, as defined by high solar reflectance and high sky window emissivity. At 150 microns thickness, the coating achieved a solar reflectance of 97.9% and a sky window emittance of 0.83. These are highly competitive values compared to others reported for greater coating thickness, and among coating and non-coating solutions for radiative cooling that have previously been developed. The weight is only 0.029 g/cm^2 due to low density of the hBN nanoplatelets and the acrylic matrix, a porosity of 44.3%, and the thinness of the paint layer. The thickness and weight represent significant reductions from previous records for radiative cooling paints. Furthermore, this paint yields an average of 6-8°C cooling below ambient. These results were due to the nanoplatelet morphology, moderately high electron bandgap of the hBN filler at 5.96 eV which eliminates UV absorption and yields higher refractive index, nanoporous nature, as well as the high concentration within the acrylic matrix at 60% volume loading. An average size in the neighborhood of peak solar wavelength and a broad size distribution also contribute to the high solar reflectance considerably. Abrasion, viscosity, and water resistance testing demonstrate that the paint is durable for outdoor use relative to other coatings and possesses a low viscosity that gives it a high degree of versatility when it comes to application techniques. The low density of the hBN nanoplatelets and the acrylic matrix, and the porosity of 44.3% help to achieve a coating paint that is thin and lightweight. It could better enable practical applications such as on buildings and automobiles, and light-weight applications such as on aircraft and fabrics.

Experimental Procedures

Resource Availability

Lead Contact

X.R. is lead contact; email address: ruan@purdue.edu

Materials Availability

hBN-Acrylic Paints generated in this study may be made available on request.

Data and Code Availability

All data and original codes mentioned in this study will be made available upon request from the research community.

hBN Nanoplatelet-Acrylic Paint Sample Fabrication

PCTP2 hBN nanoplatelets were acquired from Saint Gobain Advanced Ceramics, LLC and added in small quantities to DMF while stirring until all hBN was incorporated. The DMF solvent was used to lower viscosity of the material. The mixture was sonicated for 5 minutes to ensure uniform nanoplatelet distribution. Elvacite 2028 Acrylic powder from Lucite International, the chosen matrix material for its low viscosity, was then gradually added to the mixture while stirring until dissolved fully. The overall solid-liquid ratio is 1:6. To help with the high viscosity of the material, the stir plate was used to heat it slightly to 30°C. This final mixture was sonicated once again for 10 minutes to ensure uniformity. Samples were poured in even layers onto 1 mm thick glass slides, or 1-mm aluminum plates and left in a hood for a minimum of 6 hours to allow the DMF solvent to fully evaporate. The thickness of the samples was measured at several locations using a caliper and/or profilometer.

Porosity Calculation

The porosity of the final, dry material is calculated based on

$$\%\ Porosity = \left(1 - \frac{Solid\ Sample\ Volume}{Total\ Sample\ Volume}\right) * 100$$

Three samples were measured to determine the sample mass and calculate the solid sample volume. The samples were made by pouring the paint to fully cover 50 mm x 75 mm glass slide substrates with a consistent layer. The total sample volume for each sample was calculated by measuring the thickness of the poured layer once dry and multiplying by the area of the glass slide. The solid density was calculated using the known density of the acrylic binder, 1.185 g/cm^3, and the hBN nanoplatelets, 2.1 g/cm^3, as well as the known volume ratio of acrylic : hBN = 4 : 6. Finally, the measured sample mass and solid density is used to calculate the solid sample volume after measuring the total mass of each sample and subtracting the mass of the glass slide substrate. Using these values, the average porosity of a dried paint layer is calculated to be 44.3% with a standard deviation of 1.4%.

Estimate of Backscattering Coefficient

Mie theory is an analytical solution and is widely used for the calculation of the scattering of a plane electromagnetic wave by homogeneous spherical particles and infinite cylinders. A different method is needed for better approximation of the scattering coefficient and the asymmetry parameter of platelet particles, such as hBN nanoplatelets. In this work we solve Maxwell's equation by using Finite Element Method (FEM) and COMSOL Multiphysics.

For a homogeneous and linear medium, the electric field ($\boldsymbol{E}$) in the frequency domain is given as

$$\nabla \times (\nabla \times \boldsymbol{E}) - k_0^2 \epsilon_r \boldsymbol{E} = \boldsymbol{0}$$

where k_0 is the wavenumber in free space and ϵ_r is the relative permittivity. The light wave is mathematical approximated by a plane wave with the boundary condition

$$\boldsymbol{n} \times [\nabla \times (\boldsymbol{E} + \boldsymbol{E_b})] - jk\, \boldsymbol{n} \times (\boldsymbol{E} \times \boldsymbol{n}) = \boldsymbol{0}$$

where k is the wavenumber $\boldsymbol{E_b}$ is the scattered field defined as $\boldsymbol{E_b} = E_0 \exp\left(-\frac{2\pi jz}{\lambda}\right) \hat{\boldsymbol{x}}$, E_0 is the electric field magnitude, and λ is the wavelength.

The cross-section scattering (σ_{sc}) and the asymmetry parameter (g) are defined as

$$\sigma_{sc} = \frac{\iint_S \boldsymbol{n} \cdot \boldsymbol{P}\, dS}{S_{in}} \text{ and}$$

$$g = \frac{\iint_S \cos\theta (\boldsymbol{n} \cdot \boldsymbol{P})\, dS}{\iint_S \boldsymbol{n} \cdot \boldsymbol{P}\, dS},$$

where $\boldsymbol{P}$ is the power flow, $S_{in} = \frac{E_0^2}{2Z_0}$, Z_0 is the impedance of free space and $\cos\theta = \boldsymbol{n} \cdot \boldsymbol{k}$. From these values, the total and back scattering coefficients can be estimated (Bohren and Huffman ,1998). Validation of this model is included in Figure S2.

Spectral Characterization

The optical properties of the samples were characterized in both the UV-Vis-NIR and IR wavelengths using spectrometers. For the UV-Vis-NIR characterization, a Perkin Elmer Lambda 950 spectrometer with an integrating sphere was used along with a Spectralon diffuse reflectance standard. The characterization in the IR wavelengths was performed on a Nicolet iS50 FTIR spectrometer with a PIKE integrating sphere and a PIKE Technologies diffuse reflectance standard. A 1 mm thick glass plate substrate was used for the UV-Vis-NIR measurements to prevent contribution of the substrate to reflectance, and a 1-mm thick aluminum sheet substrate was used for the IR measurements to avoid contribution of the substrate to emissivity. Although a freestanding sample or IR-transparent substrate is preferred for sky window emissivity measurements, this was not successfully attained at this point yet and will be attempted in the future. The spectral reflectance $R\lambda$ and transmittance $T\lambda$ from 0.25-20 microns were measured and quantified, and the spectral absorptance $A\lambda$ was calculated from measured values by $A\lambda = 1 - R\lambda - T\lambda$. The sky window emissivity was calculated by first obtaining the absorptance at each

wavelength from the measured reflectance and transmittance values, and then finding the total absorptance within the sky window, pertaining to 8-13 micron wavelengths.

Field Test of Radiative Cooling Performance

The radiative cooling performance of the samples is characterized by simultaneously monitoring sample temperature, ambient temperature, and solar irradiation. The outdoor experiment was conducted at West Lafayette, IN (40.4237° N, 86.9212° W) between July 25th-28th, 2021. Figure 4a demonstrates the outdoor cooling setup. T-type thermocouples were attached to the back of the samples and suspended underneath the table to monitor the sample and ambient temperatures. The samples were placed in an insulating Styrofoam box and covered by a 12 μm PE film to mitigate conduction and convection loss without blocking the radiative heat exchange. The ambient temperature was used to calculate cooling below ambient, as using air temperature in the sample compartment would overestimate the cooling capacity and weather station temperature would underestimate it. The solar irradiation is monitored by a pyranometer. The data collection occurred every minute and a moving average of 10 minutes intervals is plotted.

Durability Characterization

The durability properties of the samples were characterized to represent various conditions representative of real-world use and application. Abrasion tests were conducted using a Taber Abraser Research Model and performed following ASTM D4060 guidelines (ASTM Subcommittee D01.23, 2010). Two CS-10 abrasive wheels with a loading of 250 grams per wheel were placed on the surface of a 150 micron thick layer of coating on a 1 mm flat aluminum sheet. The samples were weighed prior to testing, and reweighed every 250 cycles to quantify mass loss. According to the ASTM D4060 standard, the wheels were also resurfaced every 500 cycles for

consistency. Mass loss was measured over a total 2000 of cycles. Overall wear was compared with coatings commonly used in similar applications.

In order to characterize the usability for various application techniques, the viscosity of the 60% hBN-Acrylic coating was also measured across using a RheoSense Inc. microviscometer. At a consistent sample temperature of 23 °C, the viscosity of a 50 microliter sample of coating was measured across 5 discrete shear rates over a range of 50-500 s^{-1}. The results were compared with coatings commonly used in similar applications.

The potential effects of rain and other water exposure were also considered by following water resistance testing of coatings techniques as described in ASTM D870 (ASTM Subcommittee D01.27, 2020). A 2 by 2 inch 1-mm thick flat aluminum sheet was coated with 150 microns of hBN-Acrylic paint. The sample was then held in place fully submerged in a large container of gently circulating water (stirred at 280 rpm) with no contact with container walls. This setup was left in place for 24 hours, with mass of sample being measured before testing. The mass was once again measured after allowing sample to dry for 24 hours in a fume hood and the net mass loss was calculated.

Acknowledgements

The authors thank Jennifer Cahillane and Richard Smith at Purdue University for their assistance with sample fabrication, characterization, and measurements. The authors also thank Saint Gobain Advanced Ceramics LLC for donating the hBN materials. A.F. acknowledges the support from the US National Science Foundation through a Graduate Research Fellowship. I.K., Y.Z. and X.R. acknowledge partial support from the US National Science Foundation through Award #2102645.

Author Contributions

Conceptualization, X.R., G.C; methodology, X.R., G.C., A.F, I.K., Y.Z., F.B, Z.G.; investigation, A.F., I.K., F.B, Y.Z., Z.G., and J.P.; writing (original draft) A.F., I.K.; writing (review and editing), X.R., G.C. A.F, I.K., F.B., Y.Z., Z.G., and J.P.; resources, X.R. and G.C.; and supervision, X.R. and G.C. The manuscript was written through contributions of all authors. All authors have given approval to the final version of the manuscript.

Declaration of Interests

X.R., G.C. and A.F., and I.K. are inventors of a provisional patent based on this work filed with the United States Patent & Trademark Office (USPTO) on August 28, 2021. The application number is 63238124.

INCLUSION AND DIVERSITY

One or more of the authors of this paper self-identifies as an underrepresented ethnic minority in their field of research or within their geographical location. One or more of the authors of this paper self-identifies as a gender minority in their field of research. One or more of the authors of this paper received support from a program designed to increase minority representation in their field of research.

References

1. US Department of Energy. Air Conditioning. https://www.energy.gov/energysaver/air-conditioning.
2. Barker, R. (1875). The Process of making Ice in the East-Indies. Scientific American 13, 75-75. 10.1098/rstl.1775.0023.

3. Munday, J.N. (2019). Tackling Climate Change through Radiative Cooling. Joule, 3(9), pp.2057–2060. doi:10.1016/j.joule.2019.07.010.
4. Harrison, A.W. and Walton, M.R. (1978). Radiative cooling of TiO_2 white paint. Solar Energy, 20(2), pp.185–188. doi:10.1016/0038-092x(78)90195-0.
5. Orel, B., Gunde, M.Klanjšek. and Krainer, A. (1993). Radiative cooling efficiency of white pigmented paints. Solar Energy, 50(6), pp.477–482. doi:10.1016/0038-092x(93)90108-z.
6. Pockett, J. (2010). Heat Reflecting Paints and a Review of Their Advertising Material. In Chemeca 2010: Engineering at the Edge; Hilton Adelaide: South Australia. pp.1−13.
7. Holynska, M., Butenko, Y., Martins, R., Semprimoschnig, C., Meyer, F. and Faber, S. (2019). Studies of White Ceramic Coatings for ESA's BepiColombo Mission to Mercury. Journal of Spacecraft and Rockets, 56(5), pp.1358–1370. doi:10.2514/1.a34230.
8. Raman, A.P., Anoma, M.A., Zhu, L., Rephaeli, E. and Fan, S. (2014). Passive radiative cooling below ambient air temperature under direct sunlight. Nature, 515(7528), pp.540–544. doi:10.1038/nature13883.
9. Kou, J., Jurado, Z., Chen, Z., Fan, S. and Minnich, A.J. (2017). Daytime Radiative Cooling Using Near-Black Infrared Emitters. ACS Photonics, 4(3), pp.626–630. doi:10.1021/acsphotonics.6b00991.
10. Zhai, Y., Ma, Y., David, S.N., Zhao, D., Lou, R., Tan, G., Yang, R. and Yin, X. (2017). Scalable-manufactured randomized glass-polymer hybrid metamaterial for daytime radiative cooling. Science, 355(6329), pp.1062–1066. doi:10.1126/science.aai7899.
11. Li, T., Zhai, Y., He, S., Gan, W., Wei, Z., Heidarinejad, M., Dalgo, D., Mi, R., Zhao, X., Song, J., Dai, J., Chen, C., Aili, A., Vellore, A., Martini, A., Yang, R., Srebric, J., Yin, X.

and Hu, L. (2019). A radiative cooling structural material. Science, 364(6442), pp.760–763. doi:10.1126/science.aau9101.

12. Yang, Z., Zhou, Z., Sun, H., Chen, T. and Zhang, J. (2021). Construction of a ternary channel efficient passive cooling composites with solar-reflective, thermoemissive, and thermoconductive properties. Composites Science and Technology, 207, p.108743. doi:10.1016/j.compscitech.2021.108743.
13. Li, P., Wang, A., Fan, J., Kang, Q., Jiang, P., Bao, H. and Huang, X. (2021). Thermo-Optically Designed Scalable Photonic Films with High Thermal Conductivity for Subambient and Above-Ambient Radiative Cooling. Advanced Functional Materials, 32(5), p.2109542. doi:10.1002/adfm.202109542.
14. Rephaeli, E., Raman, A. and Fan, S. (2013). Ultrabroadband Photonic Structures To Achieve High-Performance Daytime Radiative Cooling. Nano Letters, 13(4), pp.1457–1461. doi:10.1021/nl4004283.
15. Huang, Z. and Ruan, X. (2017). Nanoparticle embedded double-layer coating for daytime radiative cooling. International Journal of Heat and Mass Transfer, 104, pp.890–896. doi:10.1016/j.ijheatmasstransfer.2016.08.009.
16. Atiganyanun, S., Plumley, J.B., Han, S.J., Hsu, K., Cytrynbaum, J., Peng, T.L., Han, S.M. and Han, S.E. (2018). Effective Radiative Cooling by Paint-Format Microsphere-Based Photonic Random Media. ACS Photonics, 5(4), pp.1181–1187. doi:10.1021/acsphotonics.7b01492.
17. Mandal, J., Fu, Y., Overvig, A.C., Jia, M., Sun, K., Shi, N.N., Zhou, H., Xiao, X., Yu, N. and Yang, Y. (2018). Hierarchically porous polymer coatings for highly efficient passive

daytime radiative cooling. Science, [online] 362(6412), pp.315–319. doi:10.1126/science.aat9513.

18. Peoples, J., Li, X., Lv, Y., Qiu, J., Huang, Z. and Ruan, X. (2019). A strategy of hierarchical particle sizes in nanoparticle composite for enhancing solar reflection. International Journal of Heat and Mass Transfer, 131, pp.487–494. doi:10.1016/j.ijheatmasstransfer.2018.11.059.
19. Ruan, X., Peoples, J., Li, X., Huang, Z. (2020). Metal-Free Solar-Reflective Infrared-Emissive Paints and Methods Of Producing The Same. US Patent and Trademark Office, International Application No. PCT/US2019/054566.
20. Li, X., Peoples, J., Huang, Z., Zhao, Z., qiu and Ruan, X. (2020). Full Daytime Sub-Ambient Radiative Cooling with High Figure of Merit in Commercial-Like Paints. SSRN Electronic Journal. doi:10.2139/ssrn.3652325.
21. Li, X., Peoples, J., Yao, P. and Ruan, X. (2021). Ultrawhite BaSO4 Paints and Films for Remarkable Daytime Subambient Radiative Cooling. ACS Applied Materials & Interfaces, 13(18), pp.21733–21739. doi:10.1021/acsami.1c02368.
22. Mandal, J., Yang, Y., Yu, N. and Raman, A.P. (2020). Paints as a Scalable and Effective Radiative Cooling Technology for Buildings. Joule, 4(7), pp.1350–1356. doi:10.1016/j.joule.2020.04.010.
23. Tong, Z., Peoples, J., Li, X., Yang, X., Bao, H. and Ruan, X. (2022). Electronic and phononic origins of BaSO4 as an ultra-efficient radiative cooling paint pigment. Materials Today Physics, 24, p.100658. doi:10.1016/j.mtphys.2022.100658.

24. McKay, M.A., Li, J., Lin, J.Y. and Jiang, H.X. (2020). Anisotropic index of refraction and structural properties of hexagonal boron nitride epilayers probed by spectroscopic ellipsometry. Journal of Applied Physics, 127(5), p.053103. doi:10.1063/1.5134908.
25. Lee, S., Jeong, T., Jung, S. and Yee, K. (2018). Refractive Index Dispersion of Hexagonal Boron Nitride in the Visible and Near-Infrared. physica status solidi (b), 256(6), p.1800417. doi:10.1002/pssb.201800417.
26. Golla, D., Chattrakun, K., Watanabe, K., Taniguchi, T., LeRoy, B.J. and Sandhu, A. (2013). Optical thickness determination of hexagonal boron nitride flakes. Applied Physics Letters, 102(16), p.161906. doi:10.1063/1.4803041.
27. ASTM Subcommittee D01.27 (2020). Standard Practice for Testing Water Resistance of Coatings Using Water Immersion. ASTM Book of Standards, vol. 6.01.
28. Whittingstall, P. (2011). Paint Evaluation Using Rheology. TA Instruments Thermal Analysis and Rheology, vol. RH 059
29. Bohren, C.F. and Huffman, D.R. (1998). Absorption and scattering of light by small particles. Weinheim, Germany: Wiley, pp 82-157.
30. ASTM Subcommittee D01.23. (2010). Standard Test Method for Abrasion Resistance of Organic Coatings by the Taber Abraser. ASTM Book of Standards, vol 6.01.

Figure Titles and Legends

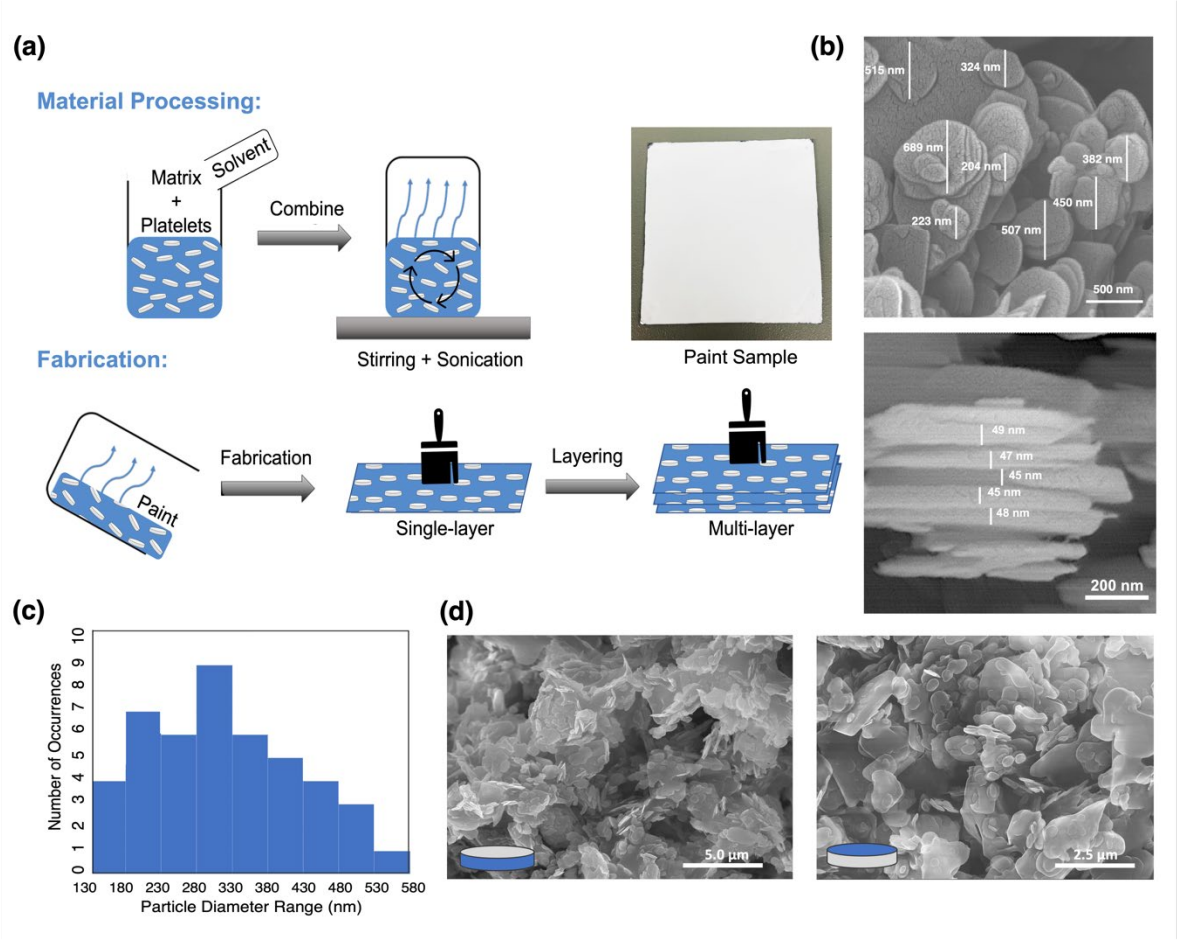

Figure 1. Radiative cooling paint preparation and characterizations. **(a)** Schematic of the hBN-Acrylic paint making process and an example image of a painted sample. **(b)** Top and side view SEM images of the hBN nanoplatelets. The nanoplatelet diameter and thickness distributions were determined to be 332 $\pm$ 193 nm and 45 $\pm$ 3 nm, respectively. **(c)** Particle diameter distribution of 50 particles demonstrated in a histogram, with the largest proportion of the diameters measured shown to be between 280-330 nm. **(d)** SEM images of hBN-Acrylic nanocomposite coating, with top-down view and cross-section view.

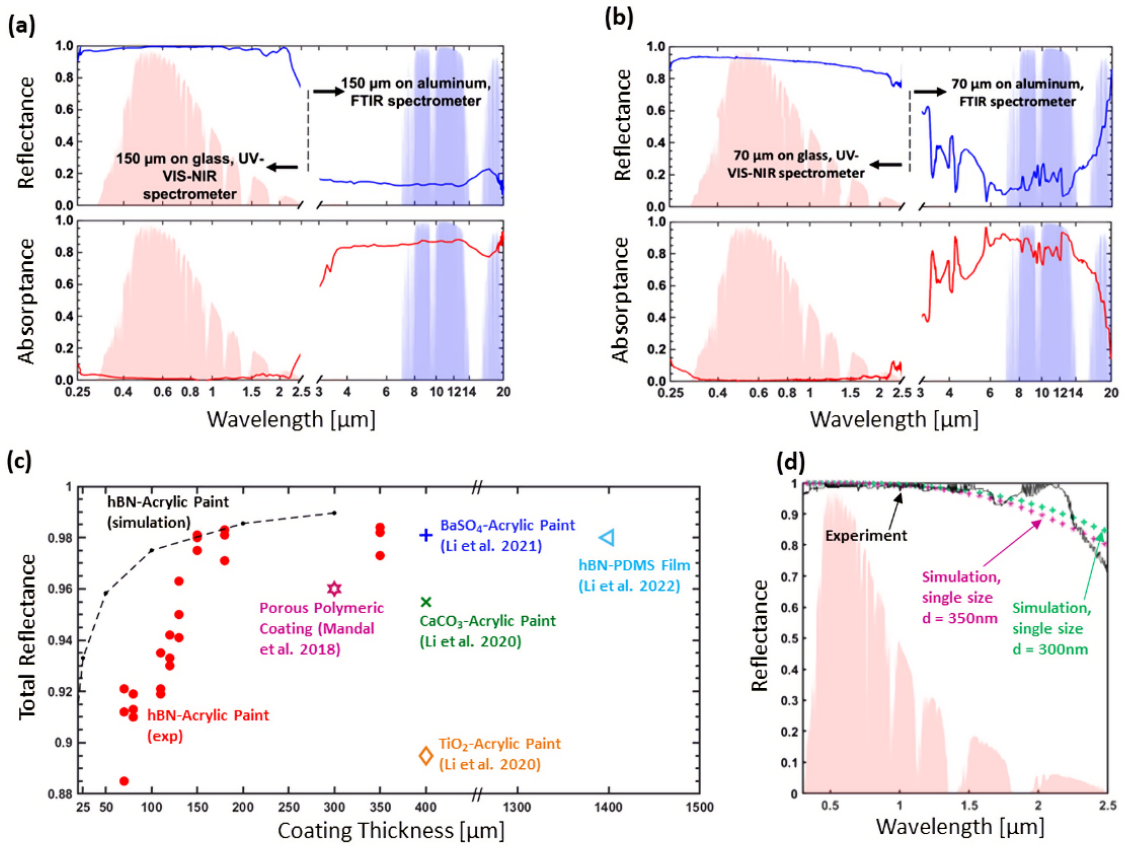

Figure 2. Spectral characterization results for hBN-Acrylic coatings of different thicknesses with various substrates and simulation results. **(a)** Spectral characterization of a 150 micron thick layer of hBN-Acrylic coating. The total solar reflectance is 97.9% and the total sky window emissivity is 0.83. Measurements from 0.25-2.5 microns were performed with a 1-mm thick glass substrate to avoid reflectance from the substrate, and measurements from 2.5-20 microns were performed with a 1-mm thick aluminum substrate to avoid emissivity contribution from the substrate. **(b)** Spectral characterization of a 70 micron thick layer of hBN-Acrylic coating. The total solar reflectance is 90.9% and the total sky window emissivity is 0.78. **(c)** The total solar reflectance as a function of the coating thicknesses. All hBN-Acrylic paint samples (red dots) were measured on 1 mm thick glass substrates. The simulated total reflectance (dashed line) as a function of the nanocomposite's thickness is calculated via Monte Carlo method. Previous literature data are also provided here, as well as given in Table 1. **(d)** Solar reflectance of hBN-Acrylic, the simulation results agree well with the experiments. Two different single sizes were used, diameters of 300nm and 350nm.

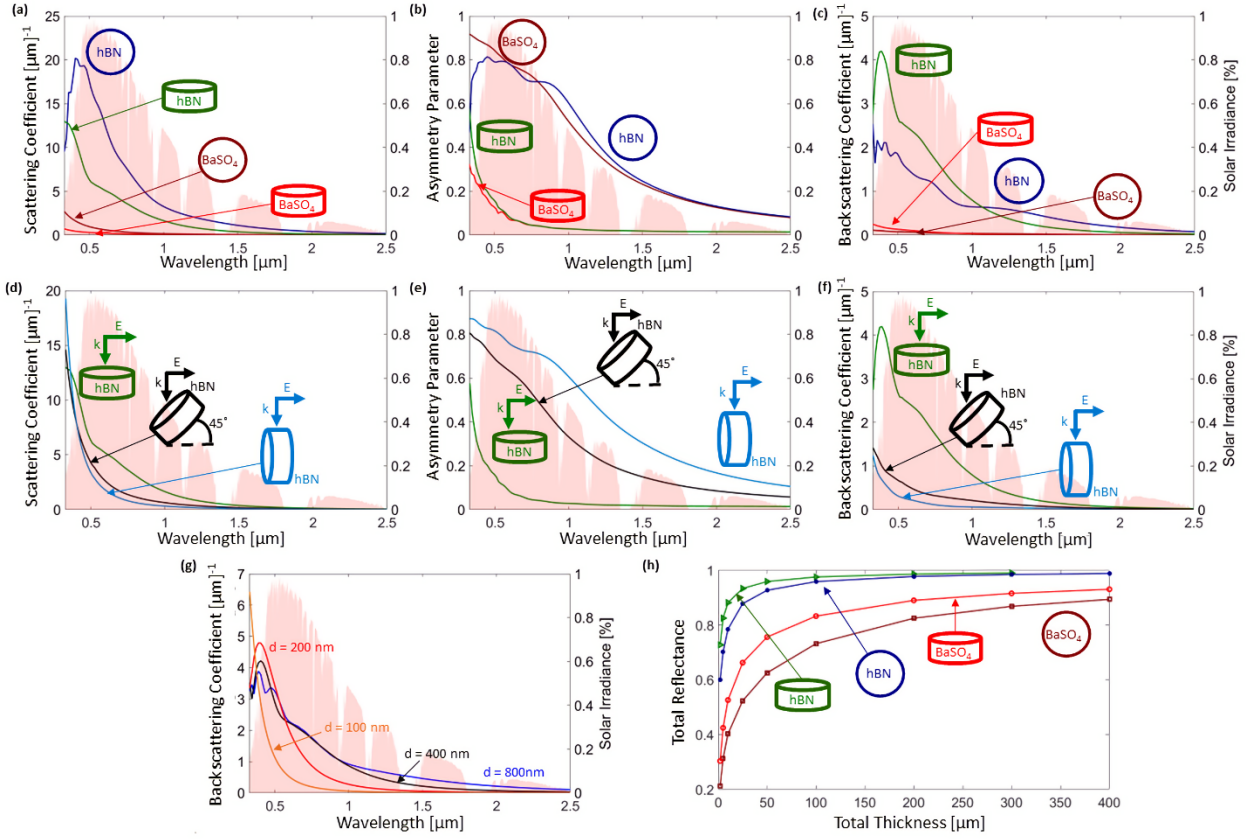

Figure 3. Simulations of the optical properties of various particles and the total reflectance of nanocomposites. **(a)** Scattering coefficient of four different particles, with different morphology and refractive index. The spherical $BaSO_4$ (brown), the platelet hBN (green), the platelet $BaSO_4$ (red) and the spherical hBN (blue). The refractive index of BaSO4 and hBN are given in Figure S1. **(b)** Asymmetry parameter of the four particles. **(c)** The backscattering coefficient of the four particles. **(d)** The scattering coefficient of platelet hBN with varying orientations, in-plane (green), 45 degrees (black) and cross-plane (light blue). **(e)** The asymmetry of platelet hBN with varying orientations. **(f)** The backscattering coefficient of platelet hBN with varying orientations. **(g)** The backscattering coefficient of hBN with different diameters of 100, 200, 400 and 800 nm. **(h)** The predicted total reflectance as a function of the total coating thickness of the four different particles. The spherical $BaSO_4$ (brown) and the platelet hBN (green), as well as the two imaginary particles, the platelet $BaSO_4$ (red) and the spherical hBN (blue).

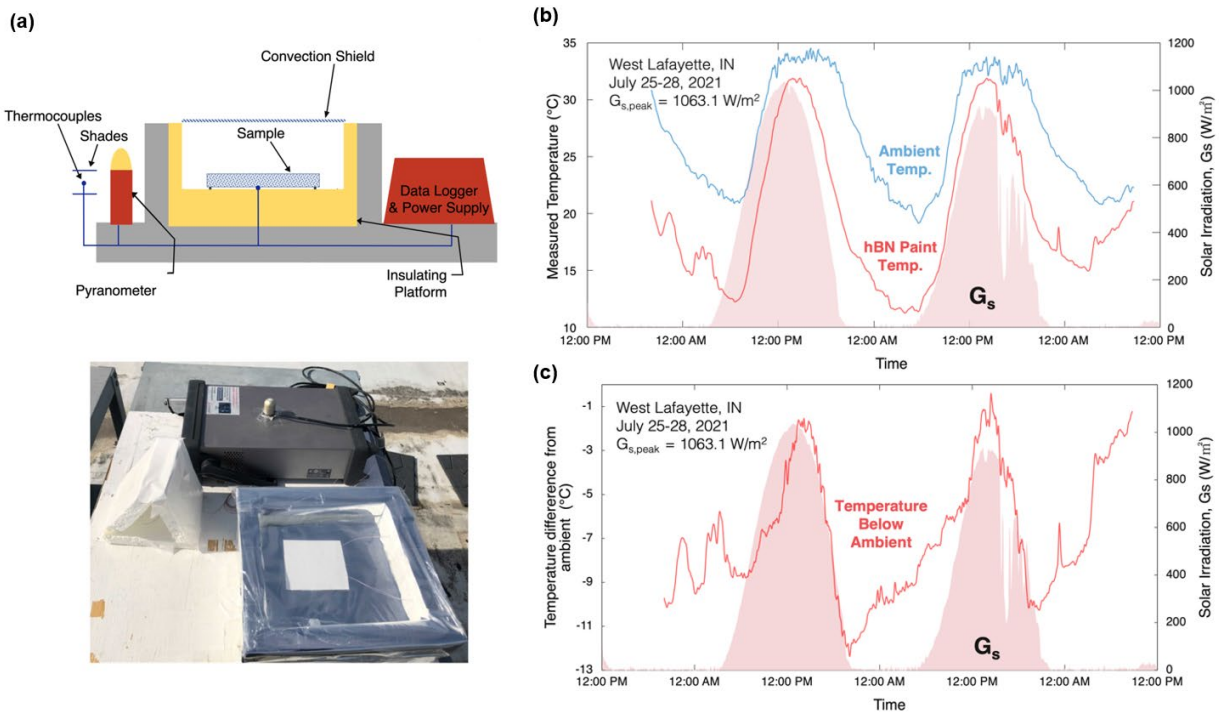

Figure 4. Field test setup and results. **(a)** Schematic and photo of the field test setup. Sample is placed in a Styrofoam insulating platform to reduce ground heating effects and 2 vertical and 1 horizontal transparent shield, made from thin polyethylene film are used around the sample to reduce forced convection loss. T-type thermocouples are used to collect temperature data of the bottom of sample, which is raised from the platform to avoid conduction loss, and the ambient, which is captured using a shaded thermocouple to avoid falsely high ambient temperature data from thermocouple overheating. The direct and diffuse solar irradiation is captured by the pyranometer. **(b)** Temperature over time of the sample surface, as well as of the ambient surroundings, from outdoor experiments over three consecutive days from July 25-28, 2021. The measured average dew point for this period was 19.2±1.2 ºC, and relative humidity was 72.9 ± 19.3%. The test was performed with samples with an average of 140 micron-thick 60% hBN-Acrylic coatings on 1 millimeter aluminum sheets of approximately 2 by 2 inches. Samples were coated via pouring and checked for consistency in layer thickness at several points throughout the surface. Data demonstrates moving average over 10 minute increments of the measured data. (**c**) Temperature difference between the ambient surroundings and the sample surfaces. Data demonstrates moving average over 10 minute increments of the measured data.

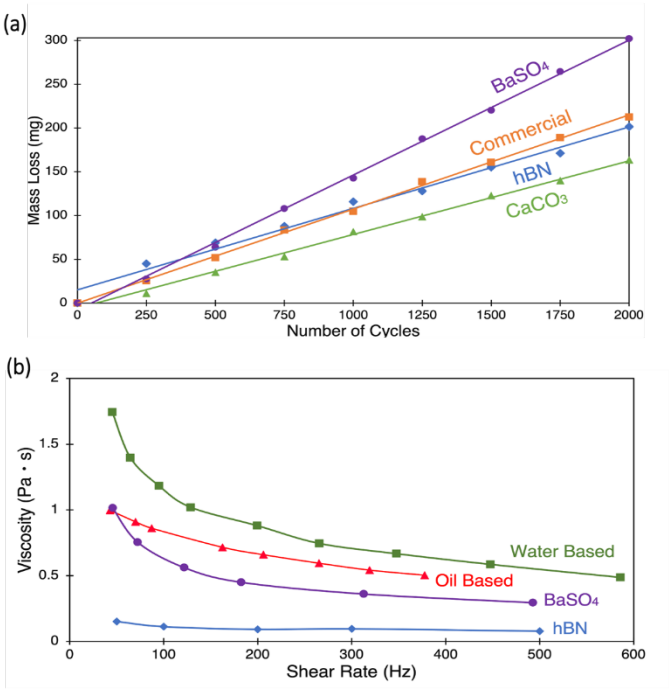

Figure 5. Results of abrasion and viscosity testing for 60% hBN-Acrylic samples with a coating thickness of 150 microns on 1-mm aluminum sheet substrates. (**a**) Abrasion testing results for hBN paint (denoted as boron nitride) compared to commercial paints (Ruan et al., 2020) and the previously developed calcite-based and barite-based paints (Li et al., 2020), (Li et al., 2021). Measurements of sample mass loss over 2000 cycles are demonstrated. (**b**) Viscosity testing for hBN (denoted as boron nitride) compared to commercial oil-based and water based paints (Bohren and Huffman, 1998) as well as the previously developed barite paint (Li et al., 2021). Measurements of the viscosity were performed at several shear rates from 10 to 600 s^{-1} for each sample.

Tables and table titles and legends

Table 1. Summary and comparison of the proposed hBN-Acrylic paint and previous radiative cooling materials in literature

Material Type	Main Component	Thickness (μm)	Total Density (g/cm^3)	Weight (g/cm^2)	Feature Size (nm)	Total Solar Reflectance	Sky Window Emissivity	RC_t
hBN-Acrylic Paint (This work)	Boron Nitride (60% volume loading)	**150**	1.9	**0.029**	332	97.9%	0.83	0.612
$BaSO_4$-Acrylic Paint (Li et al., 2021)	Barium Sulfate (60% volume loading)	400	3.34	0.134	500	98.1%	0.95	0.597
TiO2-Acrylic Paint (Li et al., 2020)	Titanium Oxide (8% volume loading)	400	3.18	0.127	100	89.5%	0.93	0.132
$CaCO_3$-Acrylic Paint (Li et al., 2020)	Calcium Carbonate (60% volume loading)	400	2.23	0.089	500	95.5%	0.94	0.453
Porous Polymeric Coating (Mandal et al., 2018)	Poly(vinylidene fluoride-co-hexafluoropropylene)	300	1.77	0.053	200, 5500	96%	0.97	0.547
hBN Photonic Film (Li et al., 2021)	Boron Nitride (40.5% volume loading)	1400	-	-	900	98%	0.89	0.05